Nano Research 2015, 8(2): 481–490
DOI 10.1007/s12274-014-0638-1
Research Article

ISSN 1998-0124
CN 11-5974/O4

Three-dimensional porous V_2O_5 hierarchical octahedrons with adjustable pore architectures for long-life lithium batteries

Qinyou An[§], Pengfei Zhang[§], Fangyu Xiong[§], Qiulong Wei, Jinzhi Sheng, Qinqin Wang, and Liqiang Mai (✉)

State Key Laboratory of Advanced Technology for Materials Synthesis and Processing, WUT–Harvard Joint Nano Key Laboratory, Wuhan University of Technology, Wuhan, Hubei 430070, China

[§] *These authors contributed equally to this work. All authors discussed the results and commented on the manuscript. The authors declare no competing financial interest.*

Received: 15 September 2014
Revised: 27 October 2014
Accepted: 12 November 2014

KEYWORDS

V_2O_5 octahedron,
adjustable pore,
long-life lithium battery

ABSTRACT

Three-dimensional (3D) porous V_2O_5 octahedrons have been successfully fabricated via a solid-state conversion process of freshly prepared ammonium vanadium oxide (AVO) octahedrons. The formation of AVO octahedrons is a result of the selective adsorption of capping reagents and the favourable supersaturation of growth species. Subsequently, 3D porous V_2O_5 octahedrons were obtained by simple thermolysis of the AVO octahedrons via a calcination treatment. As cathode material for lithium batteries, the porous V_2O_5 octahedron cathode exhibits a capacity of 96 mAh·g^{-1} at high rate up to 2 A·g^{-1} in the rang of 2.4–4 V and excellent cyclability with little capacity loss after 500 cycles, which can be ascribed to its high specific surface area and tunable pore architecture. Importantly, this facile solid-state thermal conversion strategy can be easily extended to controllably fabricate other porous metal oxide micro/nano materials with specific surface textures and morphologies.

1 Introduction

Rechargeable lithium batteries (LBs) have become a core technology for supporting the development of a sustainable and mobile society. The demand for LBs is increasing continuously due to the rapid progress of wide applications from advanced portable electronic devices to electric vehicles (EVs) and smart grids [1–6]. Superior performances in terms of energy capacity, cycling stability, and rate capability are the important factors for high-performance LBs [7–12]. Achieving breakthroughs in electrode materials is an effective approach to improved battery performance [13–21].

Among the potential cathode materials, V_2O_5 with a layered structure has been extensively studied because of its low cost, abundance, as well as its high energy efficiency and relatively high theoretical capacity (about 294 mAh·g^{-1} with 2 Li^+ ions inserted/extracted

Address correspondence to mlq518@whut.edu.cn

per unit formula) [22–26]. However, due to its slow electrochemical kinetics and poor structural stability, two major problems for this electrode material are its low rate and limited long-term cycling stability [27–29]. In order to improve these performances, many efforts have been made. Some groups prepared V_2O_5 with novel structures such as nanomaterials [30–38], hierarchical architectures [39–41], hollow microspheres [42, 43], and porous particles [44–46]. These materials showed better electrochemical performance than the pristine V_2O_5 due to the increased electrode–electrolyte contact area and reduced Li^+ diffusion distance across the electrode [33–38, 47].

Although nanostructuring has been successful in extending the electrochemical performance of V_2O_5, nanostructured electrodes have introduced new fundamental challenges, such as low tap density [48]. Additionally, some undesirable side reactions or poor thermal stability are given rise to by the extended contact between the electrolyte and the nanosized materials, which results in safety hazards and poor cycling stability [49, 50]. Generally, the method of using microsized particles is one possible approach towards high packing density and decreasing the polarization of the electrolyte in the active layer [48, 51–55].

Three dimensional (3D) porous microarchitecture electrodes have been found to enhance ion and electron transport, significantly, accommodate the volume change during lithium-ion insertion and extraction as well as facilitate electrolyte infiltration [22, 59]. Ordered superstructures consisting of nanostructures, not only maintain the nanostructural features, but also avoid some problems common to nanostructures such as low volumetric energy density and poor thermal stability [49, 50, 57].

In this work, we utilized urea as a capping reagent, and prepared 3D porous V_2O_5 octahedral microparticles successfully through a new facile route, and the dilemma of high surface area and low tap density introduced when using nanosized particles was partially solved by creating hierarchical porous microoctahedrons. To the best of our knowledge, there have been no reports of the synthesis of V_2O_5 octahedrons. When used as an cathode material for LBs, V_2O_5 octahedrons demonstrated much better cycling performance than other V_2O_5 samples (e.g. hollow spheres, nanowires), which could be attributed to their unique architecture with accessible channel structural features.

2 Experimental

2.1 Materials synthesis

In a typical synthesis, NH_4VO_3 (2 mmol) and urea (3.0 g) were dissolved in 10 mL of deionized water in turn under vigorous stirring at 80 °C. After stirring for 20 min, 1,2-propanediol (50 mL) was added into the above solution, and stirring was continued for 1 h. Subsequently, the mixture was transferred into a Teflon-lined stainless steel autoclave with a capacity of 100 mL. After heating at 180 °C for 6 h, the autoclave was naturally cooled to room temperature, and the precipitate was collected by centrifugation and washed three times with pure ethanol. Finally, 3D porous V_2O_5 octahedrons were obtained by annealing the solvothermally prepared ammonium polyvanadate ($NH_4V_3O_8$ and $(NH_4)_2V_3O_8$) octahedrons in air at 500 °C for 5 h with a heating rate of 3 °C·min^{-1}. A series of experiments were also carried out at different solvothermal reaction time and annealing temperature to study the structural evolution process.

2.2 Characterization

X-ray diffraction (XRD) measurements were performed to investigate the crystallographic information using a Bruker D8 ADVANCE X-ray diffractometer with a non-monochromated Cu Kα X-ray source. Field emission scanning electron microscopy (FESEM) images were collected with a JEOL-7100F microscopy at an acceleration voltage of 10 kV. Transmission electron microscopy (TEM), high-resolution transmission electron microscopy (HRTEM) images were recorded by using a JEM-2100F STEM/EDS microscope. Brunauer–Emmett–Teller (BET) surface areas were measured using a Tristar II 3020 instrument to measure the adsorption of nitrogen. X-ray photoelectron spectroscopy (XPS) measurements were obtained using a VG MultiLab 2000 instrument.

2.3 Measurement of electrochemical performance

The electrochemical properties were investigated by assembly of 2025 coin cells in a glove box filled with

pure argon gas, using lithium pellet as the anode, 1 M solution $LiPF_6$ in ethylene carbonate (EC)/dimethyl carbonate (DMC) as electrolyte, and cathode electrodes with 70% V_2O_5 octahedrons as the active material, 20% of acetylene black and 10% of poly(tetrafluoroethylene) (PTFE). Galvanostatic charge/discharge cycling was studied in the potential range of 4.0–2.4 V vs. Li/Li^+ with a multichannel battery testing system (LAND CT2001A). Cyclic voltammetry (CV) and AC-impedance spectra were tested with an electrochemical workstation (Autolab PGSTAT 302 and CHI 760D).

3 Results and discussion

The resulting products prepared by solvothermal synthesis were characterized by XRD to identify the crystallographic structure and crystallinity, and the diffraction patterns are presented in Fig. 1(a). It can be observed that the peaks match those of monoclinic $NH_4V_3O_8$ (JCPDS NO. 01-084-0972, space group: $P2_1/m$, a = 4.9930 Å, b = 8.4180 Å, c = 7.8580 Å) and $(NH_4)_2V_3O_8$ (JCPDS NO. 01-089-6614, space group: $P4bm$, a = 8.8910 Å, b = 8.8910 Å, c = 5.5820 Å). The strong and narrow peaks indicate the high crystallinity of the as-prepared products. Moreover, the XPS of AVO octahedrons (Fig. S1(a), in the Electronic Supplementary Material (ESM)) shows that both V^{4+} and V^{5+} exist, consistent with the XRD. As shown in the low magnification FESEM image (Fig. 1(b)), the ammonium vanadium oxide sample is composed of the octahedral particles, with a diameter range of 3–6 μm. FESEM images with a higher magnification (Figs. 1(c) and 1(d)) show that the surface of the octahedron is smooth, and the solid interior structure of the octahedrons was revealed by TEM (Fig. 1(e)), which illustrates that the ammonium vanadium oxide octahedrons are microcrystals without any elaborate inner architectures in the bulk. In addition, energy dispersive spectrometry (EDS) mapping analysis indicates that V, N and O are homogeneously distributed in the ammonium vanadium oxide octahedrons (Fig. 1(f)).

The ammonium vanadium oxide octahedrons can be easily converted into 3D porous V_2O_5 octahedrons by annealing in air. The representative XRD pattern shown in Fig. 2(a) characterizes the phase purity and crystallinity of the obtained 3D porous V_2O_5 octahedrons

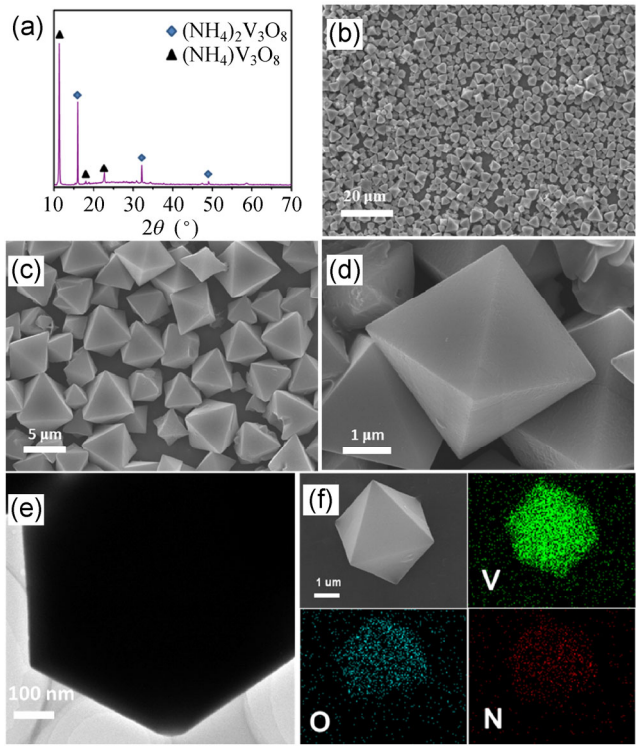

Figure 1 XRD pattern (a), FESEM images (b)–(d), TEM image (e) and EDS mapping (f) of ammonium vanadium oxide octahedrons.

calcined at 500 °C (V_2O_5-500) for 5 hours. All of the diffraction peaks can be unambiguously indexed and assigned to the orthogonal V_2O_5 phase (JCPDS NO. 00-041-1426, space group: $Pmmn$, a = 11.5160 Å, b = 3.5656 Å, c = 4.3727 Å). No other phase is detected, which indicates the high purity of the 3D porous V_2O_5 octahedrons. Moreover, the XPS of the 3D porous V_2O_5 octahedrons (Fig. S1(b) in the ESM) shows that only V^{5+} exists, consistent with the XRD. The morphology and detailed structure of the 3D porous V_2O_5 octahedrons obtained from the ammonium vanadium oxide octahedrons were further investigated by FESEM and TEM. A view of the product (Figs. 2(b) and 2(c)) reveals that a pore structure can be observed on the surface of V_2O_5 sample calcined at 500 °C and the material morphology is essentially preserved during the annealing and solid-phase conversion process, with the particles having a similar size to the pristine ammonium vanadium oxide octahedrons. There is no discernible shrinkage or structural deformation in the V_2O_5 octahedrons, which suggests excellent structural stability.

To further confirm the inner architecture and the

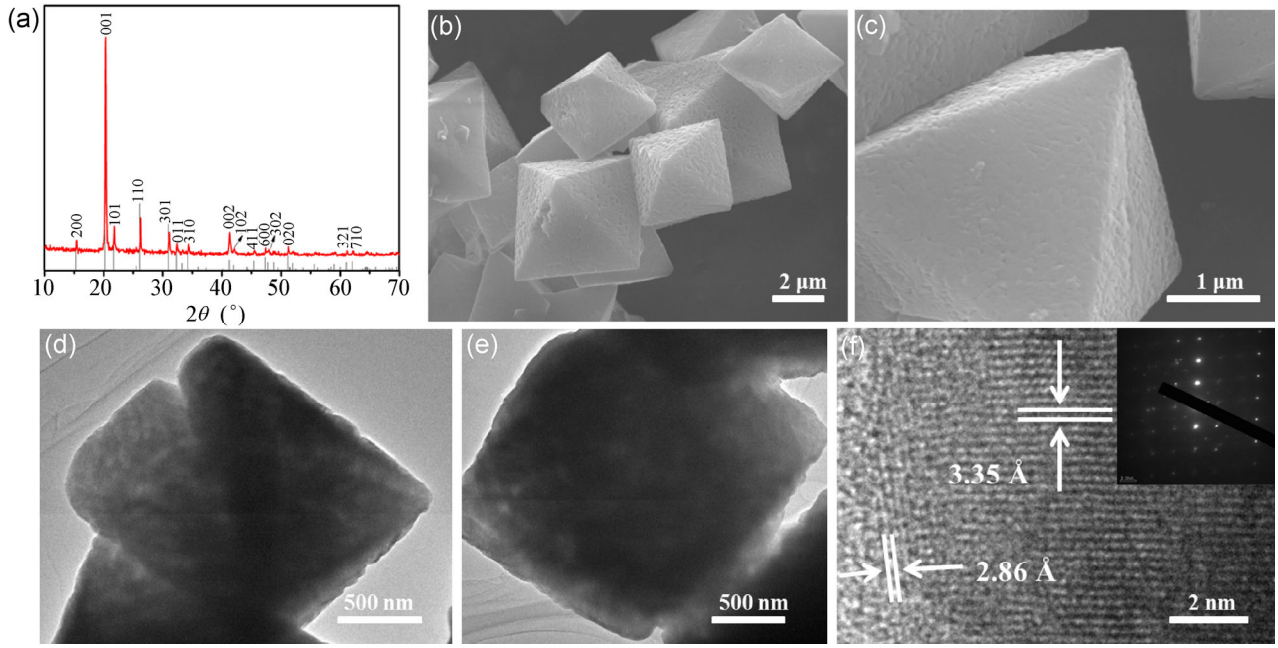

Figure 2 XRD pattern (a), FESEM images (b) and (c), TEM images (d) and (e), and HRTEM image (f) with the corresponding SAED pattern (inset) of the as-prepared 3D porous V_2O_5 octahedrons calcined at 500 °C.

crystallographic structure of the octahedral porous V_2O_5, TEM and the high-resolution transmission electron microscopic (HRTEM) were carried out. The representative TEM images (Figs. 2(d) and 2(e)) and the fracture surface FESEM images of broken octahedrons particles (Figs. S2 and S3, in the ESM) indicate that the synthesized 3D porous V_2O_5 octahedrons are actually composed of numerous nanoparticles with a mean size of 100 nm, and these particles undergo aggregation to form porous agglomerate structure. The HRTEM image (Fig. 2(f)) taken from the edge of 3D porous octahedrons shows clearly visible lattice fringes with spacings of 3.35 and 2.86 Å, corresponding to the d-spacings of the (110) and (301) planes of orthorhombic V_2O_5, respectively. The EDS mapping analysis indicates that V and O are homogeneously distributed in the 3D porous V_2O_5 octahedrons (Fig. S4, in the ESM). A schematic illustration of the synthesis of the 3D porous V_2O_5 octahedrons is shown in Fig. 3. Because of the space-efficient 3D porous octahedral microparticles, their tap density is significantly higher than the V_2O_5 nanowires. In the simplified demonstration shown in Fig. S5 (in the ESM), the V_2O_5 nanowires have a tap density of 0.73 g·cm^{-3}, while the octahedral microparticles have a tap density of 1.01 g·cm^{-3}, which represents an increase of 36%. The formation of the ammonium vanadium oxide octahedrons (Fig. 3(b)) and the control experiment without urea (Fig. S6, in the ESM) suggest that urea serves as a capping reagent, and selective adhesion of urea on the facets alters the crystal habits significantly. In addition, the octahedron-shaped morphology obtained at certain supersaturation in the presence of urea is the thermodynamically favorable one [58]. At the same time, urea adhering on the crystal shows a certain ability to dissociate particles and affect the particles' aggregation through direct binding to the particles' surface [59]. On the other hand, the hydrolysis of ammonium metavanadate is restrained effectively by the ammonia derived from urea during the solvothermal process (Eqs. (1)–(5)), leading to the ammonium vanadium oxide octahedron microstructure after solvothermal reaction. The formation of $(NH_4)_2V_3O_8$ is attributed to the oxidizing ability of 1, 2-propanediol.

$$NH_4VO_3 \rightarrow NH_4^+ + VO_3^- \quad (1)$$

$$(NH_2)_2CO + H_2O \rightarrow 2NH_3 + CO_2 \quad (2)$$

$$NH_3 + H_2O \rightarrow NH_4^+ + OH^- \quad (3)$$

$$2NH_4^+ + 3VO_3^- \rightarrow V_3O_8^- + 2NH_3 + H_2O \quad (4)$$

$$6VO_3^- + CH_2OHCHOHCH_3 + 2NH_4^+ \rightarrow 2V_3O_8^{2-} + CHOCHOHCH_3 + 2NH_3 + 2H_2O \quad (5)$$

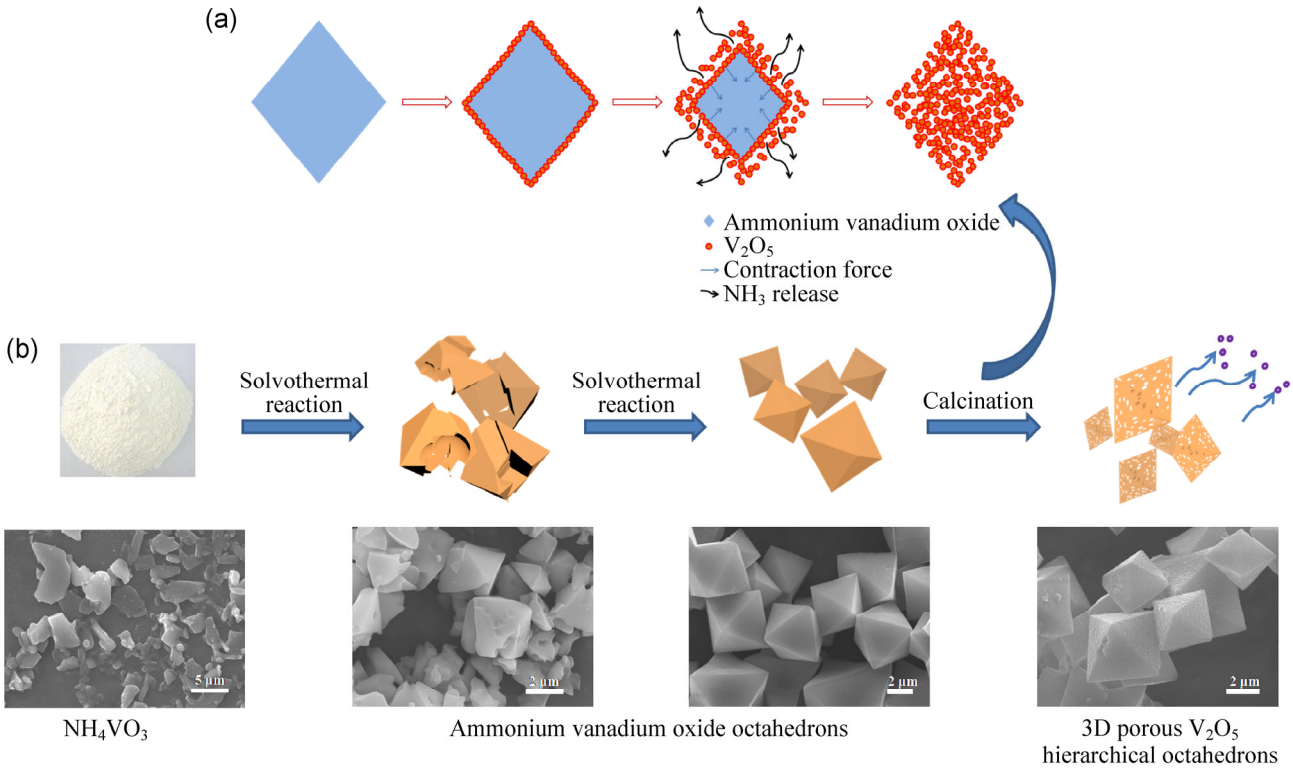

Figure 3 (a) Details of the thermal decomposition of ammonium vanadium oxide octahedrons. (b) A schematic illustration of the formation of 3D porous V_2O_5 octahedrons through a one-step thermal decomposition of ammonium vanadium oxide octahedrons.

During the process of thermolysis, the volume shrinkage and the release of internally generated ammonia (NH_3), result in the conversion from $(NH_4)_2V_3O_8$ and $NH_4V_3O_8$ to their corresponding oxides. In detail (Fig. 3(a)), the newly formed V_2O_5 layer seals in NH_3, which is very densely coated on the ammonium vanadium oxide octahedrons, blocking the gas release effectively. Subsequently, the increasing pressure attributed to the accumulated ammonia breaks up the dense V_2O_5 layer, forming a small void/pore. Many such processes can concurrently/continuously occur from the outer to the inner part of the crystals until continuous channels are eventually formed, while $(NH_4)_2V_3O_8$ and $NH_4V_3O_8$ are completely decomposed to V_2O_5 [60, 61]. Finally, the ammonium vanadium oxide octahedrons were decomposed into 3D porous V_2O_5 octahedrons by calcination processes, shown in Equations (6) and (7).

$$4(NH_4)_2V_3O_8 + O_2 \rightarrow 8NH_3 + 6V_2O_5 + 4H_2O \quad (6)$$

$$2NH_4V_3O_8 \rightarrow 2NH_3 + 3V_2O_5 + H_2O \quad (7)$$

Furthermore, according to the formation mechanism of 3D porous V_2O_5 octahedrons (Fig. 3(b)), the more violent volume shrinkage and the greater release of internally generated NH_3 facilitate the generation of channels with bigger size when the calcination temperature increases. Therefore, we achieved controllable synthesis of 3D porous V_2O_5 octahedrons with different porosity by adjusting the calcination temperature. Figure 4 shows that the 3D porous V_2O_5 octahedrons annealed at higher temperature display smaller porosity, but the morphology of the octahedral particles are not destroyed. Nitrogen adsorption–desorption isotherms were further measured to characterize the pore structure of the products. It is found that the sample calcined at 350 °C (V_2O_5-350) has a BET surface area of 17.3 $m^2 \cdot g^{-1}$ with mesopores from 2–3 to 10–40 nm on the basis of the Barrett–Joyner–Halenda (BJH) method (inset of Fig. 5(a)). The sorption isotherms of V_2O_5-350 (Fig. 5(a)) appear to be type II curves, with the H3 hysteresis loops that can be linked to slit-shaped pores. Figure 5(b) shows the pore structure characterization of the ammonium vanadium oxide octahedrons and that with increasing

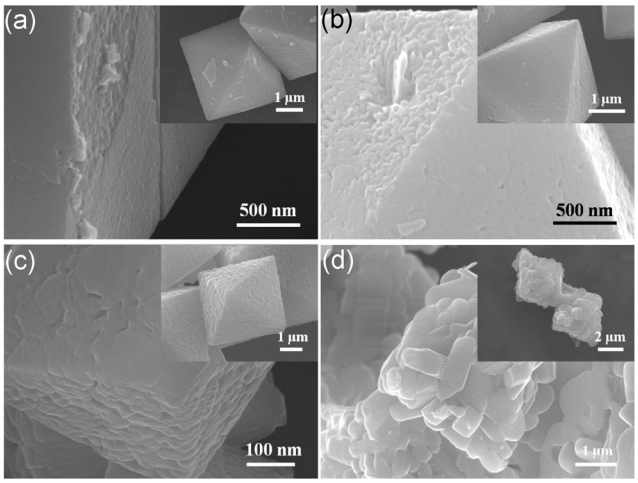

Figure 4 FESEM images of 3D porous V_2O_5 octahedrons annealed at 350 ˚C (a), 400 ˚C (b), 500 ˚C (c) and 600 ˚C (d).

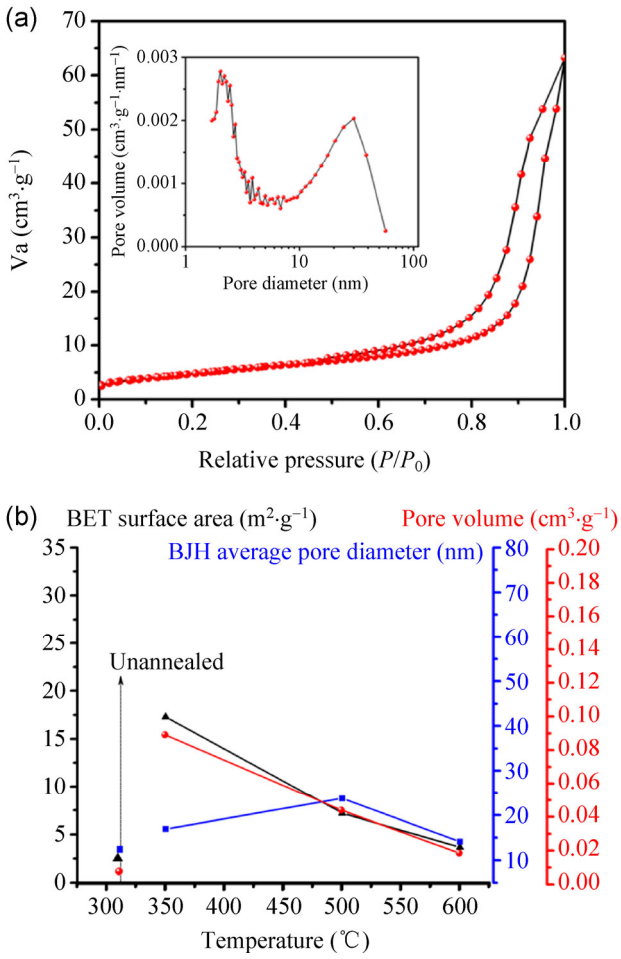

Figure 5 (a) Nitrogen adsorption–desorption isotherms of V_2O_5-350 and the corresponding pore size distribution (inset). (b) BET surface area, average pore diameter and pore volume of V_2O_5 samples with different calcination temperatures.

calcination temperature, the average pore diameter of the V_2O_5 sample increases, whereas the BET surface area and pore volume of the V_2O_5 sample decreases; this suggests that the pore structure of the products underwent a change, which is consistent with the results in Fig. 4 and Fig. S7 (in the ESM). The BET surface area of V_2O_5 annealed at 600 ˚C decreased to 3.6 $m^2 \cdot g^{-1}$, and no pore structure is present, according to the low BET surface area and absence of pore size data.

Coin cells with metallic lithium as an anode were assembled to investigate the electrochemical performance of the porous V_2O_5 octahedron cathodes of different annealing temperatures. Cyclic voltammograms (CV) of the V_2O_5 octahedrons were measured at a scan rate of 0.1 $mV \cdot s^{-1}$ in the potential range from 2.4 to 4.0 V (Fig. 6(a)). The cathodic and anodic peaks are ascribed to the lithium ion insertion and extraction, respectively. Two main cathodic peaks appear at potentials of 3.34 and 3.12 V, corresponding to the phase transformations from α-V_2O_5 to ε-$Li_{0.5}V_2O_5$ and δ-LiV_2O_5, the processes of which are expressed in Eq. (8) and (9) [59], respectively.

$$V_2O_5 + 0.5Li^+ + 0.5e^- = \varepsilon\text{-}Li_{0.5}V_2O_5 \quad (8)$$

$$\varepsilon\text{-}Li_{0.5}V_2O_5 + 0.5Li^+ + 0.5e^- = \delta\text{-}LiV_2O_5 \quad (9)$$

Figure 6(b) displays the discharge/charge curves of the V_2O_5 octahedron cathodes at a current density of 50 $mA \cdot g^{-1}$. Two voltage plateaus are clearly observed, which are quite consistent with the CV curves. The cycling performance at low current density was further evaluated by galvanostatic discharge/charge testing. As shown in Fig. 6(c), the initial discharge capacity of the 3D porous V_2O_5 octahedrons was 135 $mAh \cdot g^{-1}$ at 100 $mA \cdot g^{-1}$, although the capacity is not close to the theoretical value of 147 $mAh \cdot g^{-1}$ for the formation of δ-LiV_2O_5. After 60 cycles the discharge capacity still remains as high as 141 $mAh \cdot g^{-1}$, with no obvious capacity fading. The improvement in capacity could indicate the gradual penetration of electrolyte into the particles' interior [61].

For the purpose of applications of LBs in EVs and HEVs, good rate capability and excellent cycleability are both necessary. To evaluate the rate capability, the 3D porous V_2O_5 octahedron cathodes annealed at different temperatures were cycled at various rates, ranging from 0.1 to 2 $A \cdot g^{-1}$ (Fig. 6(d)) and the V_2O_5-350

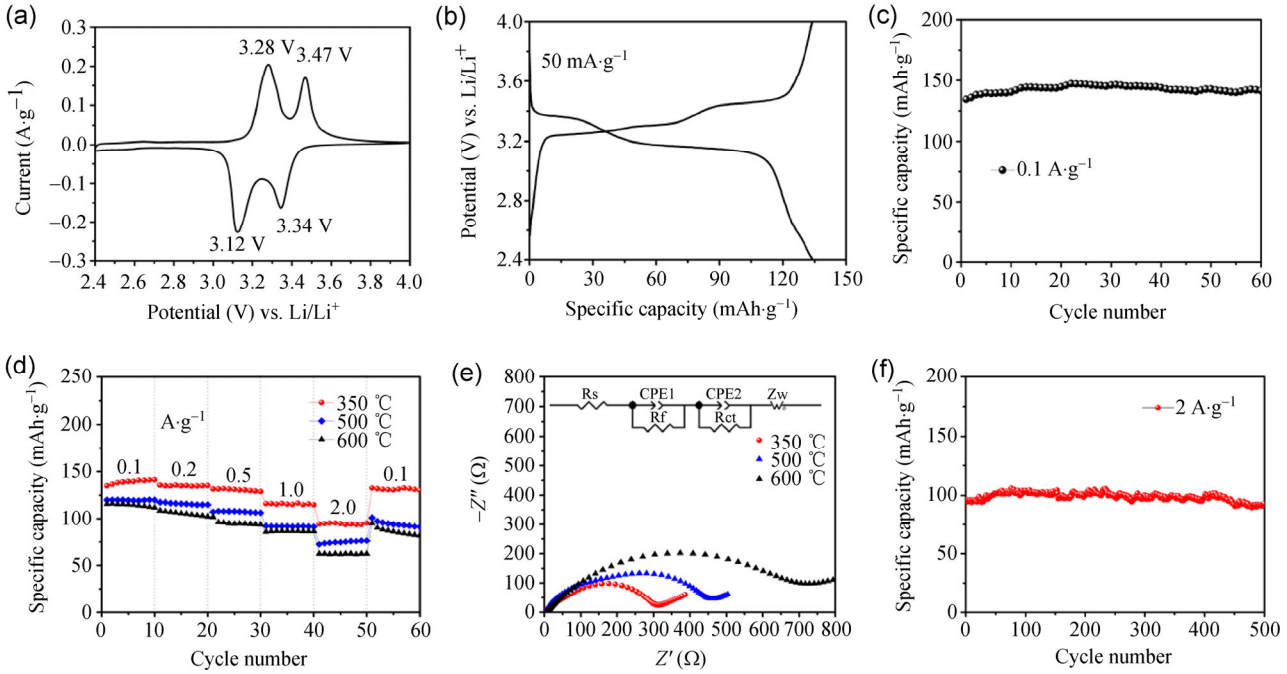

Figure 6 Electrochemical characterization of 3D porous V_2O_5 octahedrons annealed at 350 ℃: (a) Cyclic voltammograms at a scan rate of 0.1 mV·s^{-1}; (b) discharge/charge curves of the first cycle at 50 mA·g^{-1}; (c) cycling performance at a current density of 100 mA·g^{-1}; (d) the rate performance of V_2O_5 octahedron electrodes prepared at different annealing temperatures (charged at 100 mA·g^{-1}). (e) AC impedance spectra of V_2O_5 octahedron electrodes prepared at different annealing temperatures. (f) Long-term cycling performance of the V_2O_5 octahedron cathodes at a high discharge current density of 2 A·g^{-1} (charged at 100 mA·g^{-1}).

showed the best rate performance of all the products. As the current densities increase from 0.1 to 2 A·g^{-1}, the discharge capacity of the V_2O_5-350 octahedron cathodes decreases gradually from 135 to 96 mAh·g^{-1}. After the high rate measurement, when the current density was reduced back to 0.1 A·g^{-1} a discharge capacity of 133 mAh·g^{-1} was recovered. These results indicate the excellent rate capability and structural stability of V_2O_5-350 octahedrons. Electrochemical impedance spectra (EIS) were used to provide further insights (Fig. 6(e)). The Nyquist plots indicate that the charge transfer resistance (R_{ct}) of V_2O_5-350 with its higher BET surface area is 202 Ω, which is much lower than that of the other two cathodes (231 and 562 Ω), indicating that the charge-transfer process on the electrode/electrolyte interface is more facile due to the increased contact area between the electrolyte and electrode, as well as the shorter diffusion distance for Li^+ ions, giving rise to rapid ion diffusion and an efficient charge transfer [62, 63]. Moreover, the cycling performance of the V_2O_5 octahedron cathodes at a high current density of 2 A·g^{-1} was tested (Fig. 6(f)). The initial specific discharge capacity is 96 mAh·g^{-1} at this high current density, and—remarkably—a capacity as high as 93 mAh·g^{-1} was retained after 500 cycles, corresponding to 96.9% of the initial capacity. The electrochemical performance of the V_2O_5 octahedrons is good compared to that of many published V_2O_5 electrodes, in terms of high-rate capability and cycling performance (Table S1, in the ESM). The reason is probably that the specific porous space of the V_2O_5 nanoparticle aggregates with high porosity, forming a robust reservoir for Li^+ ions, thus improving the diffusion kinetics within the electrode. Furthermore, these hierarchical porous channels ensure efficient contact between the surface of the electroactive particles and the electrolyte [64, 65].

4 Conclusions

V_2O_5 octahedrons have been successfully synthesized by a facile solvothermal method followed by annealing in air. The morphology of the V_2O_5 can be controlled by introducing surfactants in the polyol process. The resulting 3D porous V_2O_5 octahedrons deliver promising Li storage properties with stable cyclabilities,

and good rate performances. They show a specific capacity of 96 mAh·g^{-1} at 2 A·g^{-1} and, remarkably, 96.9% of the initial capacity is retained after 500 cycles, which is attractive for the development of Li batteries with long-term cycling stability. The excellent cycling stability can be attributed to the unique octahedral structure. In addition, the strategy demonstrated herein is effective for the exploration of electrode materials with long-term cycling stability and paves a feasible way to the development of controllable and reproducible strategies for effectively tailoring the porosity of porous micro/nano structures for use in advanced energy storage devices.

Acknowledgements

This work was supported by the National Basic Research Program of China (2013CB934103, 2012CB933003), the National Science Fund for Distinguished Young Scholars (51425204), the National Natural Science Foundation of China (51272197), the Hubei Science Fund for Distinguished Young Scholars (2014CFA035) and the Fundamental Research Funds for the Central Universities (2013-VII-028). Thanks to Prof. C.M. Lieber of Harvard University, Prof. Dongyuan Zhao of Fudan University and Dr. Jun Liu of Pacific Northwest National Laboratory for strong support and stimulating discussion.

Electronic Supplementary Material: Supplementary material (FESEM images of V_2O_5-350 and the fracture surface, EDS mapping of V_2O_5 annealed at 500 °C, pictures of the 3D porous V_2O_5 octahedrons and V_2O_5 nanowires, FESEM images of the products after solvothermal reaction, nitrogen adsorption–desorption isotherms and corresponding pore size distribution annealed at different temperatures, cycling performance and discharge/charge curves of V_2O_5-350 and the electrochemical performances of the 3D porous V_2O_5 octahedrons and the reported V_2O_5 materials) is available in the online version of this article at http://dx.doi.org/10.1007/s12274-014-0638-1.

References

[1] Kang, B.; Ceder, G. Battery materials for ultrafast charging and discharging. *Nature* **2009**, *458*, 190–193.

[2] Armand, M.; Tarascon, J. M. Building better batteries. *Nature* **2008**, *451*, 652–657.

[3] Zu, C. X.; Li, H. Thermodynamic analysis on energy densities of batteries. *Energy Environ. Sci.* **2011**, *4*, 2614–2624.

[4] Winter, M.; Besenhard, J. O.; Spahr, M. E.; Novák, P. Insertion electrode materials for rechargeable lithium batteries. *Adv. Mater.* **1998**, *10*, 725–763.

[5] Liu, G. Q.; Wen, L.; Liu, Y. M. Spinel $LiNi_{0.5}Mn_{1.5}O_4$ and its derivatives as cathodes for high-voltage Li-ion batteries. *J. Solid State Electrochem.* **2010**, *14*, 2191–2202.

[6] Zhang, C. Z.; Mahmood, N.; Yin, H.; Liu, F.; Hou, Y. L. Synthesis of phosphorus-doped graphene and its multifunctional applications for oxygen reduction reaction and lithium ion batteries. *Adv. Mater.* **2013**, *25*, 4932–4937.

[7] Yang, S. B.; Cui, G. L.; Pang, S. P.; Cao, Q.; Kolb, U.; Feng, X. L.; Maier, J.; Müllen, K. Fabrication of cobalt and cobalt oxide/graphene composites: Towards high-performance anode materials for lithium ion batteries. *ChemSusChem* **2010**, *3*, 236–239.

[8] Whittingham, M. S. Lithium batteries and cathode materials. *Chem. Rev.* **2004**, *104*, 4271–4302.

[9] Goodenough, J. B.; Kim, Y. Challenges for rechargeable Li batteries. *Chem. Mater.* **2010**, *22*, 587–603.

[10] Tarascon, J. M.; Armand, M. Issues and challenges facing rechargeable lithium batteries. *Nature* **2001**, *414*, 359–367.

[11] Wu, H.; Chan, G.; Choi, J. W.; Yao, Y.; McDowell, M. T.; Lee, S. W.; Jackson, A.; Yang, Y.; Hu, L. B.; Cui, Y. Stable cycling of double-walled silicon nanotube battery anodes through solid-electrolyte interphase control. *Nat. Nanotechnol.* **2012**, *7*, 310–315.

[12] Jiang, J.; Feng, Y.; Mahmood, N.; Liu, F.; Hou, Y. L. SnS_2/graphene composites: Excellent anode materials for lithium ion battery and photolysis catalysts. *Sci. Adv. Mater.* **2013**, *5*, 1667–1675.

[13] Wang, Y. G.; Li, H. Q.; Xia, Y. Y. Ordered whiskerlike polyaniline grown on the surface of mesoporous carbon and its electrochemical capacitance performance. *Adv. Mater.* **2006**, *18*, 2619–2623.

[14] Yao, Y.; McDowell, M. T.; Ryu, I.; Wu, H.; Liu, N.; Hu, L. B.; Nix, W. D.; Cui, Y. Interconnected silicon hollow nanospheres for lithium-ion battery anodes with long cycle life. *Nano Lett.* **2011**, *11*, 2949–2954.

[15] Li, L.; Fang, X. S.; Chew, H. G.; Zheng, F.; Liew, T. H.; Xu, X. J.; Zhang, Y. X.; Pan, S. S.; Li, G. H.; Zhang, L. Crystallinity-controlled germanium nanowire arrays: Potential field emitters. *Adv. Funct. Mater.* **2008**, *18*, 1080–1088.

[16] Hassoun, J.; Derrien, G.; Panero, S.; Scrosati, B. A nanostructured Sn–C composite lithium battery electrode with unique stability and high electrochemical performance. *Adv. Mater.* **2008**, *20*, 3169–3175.

[17] Sun, Y. M.; Hu, X. L.; Luo, W.; Xia, F. F.; Huang, Y. H. Reconstruction of conformal nanoscale MnO on graphene as a high-capacity and long-life anode material for lithium ion batteries. *Adv. Funct. Mater.* **2013**, *23*, 2436–2444.

[18] Cao, Y. L.; Li, X. L.; Aksay, I. A.; Lemmon, J.; Nie, Z. M.; Yang, Z. G.; Liu, J. Sandwich-type functionalized graphene sheet–sulfur nanocomposite for rechargeable lithium batteries. *Phys. Chem. Chem. Phys.* **2011**, *13*, 7660–7665.

[19] Fergus, J. W. Recent developments in cathode materials for lithium ion batteries. *J. Power Sources* **2010**, *195*, 939–954.

[20] Chen, J.; Xu, L. N.; Li, W. Y.; Gou, X. L. α-Fe_2O_3 nanotubes in gas sensor and lithium-ion battery applications. *Adv. Mater.* **2005**, *17*, 582–586.

[21] Mahmood, N.; Zhang, C. Z.; Jiang, J.; Liu, F.; Hou, Y. L. Multifunctional Co_3S_4/graphene composites for lithium ion batteries and oxygen reduction reaction. *Chem. Eur. J.* **2013**, *19*, 5183–5190.

[22] Wang, S. Q.; Li, S. R.; Sun, Y.; Feng, X. Y.; Chen, C. H. Three-dimensional porous V_2O_5 cathode with ultra high rate capability. *Energy Environ. Sci.* **2011**, *4*, 2854–2857.

[23] Qu, Q. T.; Zhu, Y.; Gao, X.; Wu, Y. S. Core–shell structure of polypyrrole grown on V_2O_5 nanoribbon as high performance anode material for supercapacitors. *Adv. Energy Mater.* **2012**, *2*, 950–955.

[24] Xie, J.; Yang, X. G.; Zhou, S.; Wang, D. W. Comparing one- and two-dimensional heteronanostructures as silicon-based lithium ion battery anode materials. *ACS nano* **2011**, *5*, 9225–9231.

[25] Wang, Y.; Cao, G. Z. Developments in nanostructured cathode materials for high-performance lithium-ion batteries. *Adv. Mater.* **2008**, *20*, 2251–2269.

[26] Zhai, T. Y.; Ye, M. F.; Li, L.; Fang, X. S.; Liao, M. Y.; Li, Y. F.; Koide, Y.; Bando, Y.; Golberg, D. Single-crystalline Sb_2Se_3 nanowires for high-performance field emitters and photodetectors. *Adv. Mater.* **2010**, *22*, 4530–4533.

[27] Ban, C. M.; Chernova, N. A.; Whittingham, M. S. Electrospun nano-vanadium pentoxide cathode. *Electrochem. Commun.* **2009**, *11*, 522–525.

[28] Muster, J.; Kim, G. T.; Krstić, V.; Park, J. G.; Park, Y. W.; Roth, S.; Burghard, M. Electrical transport through individual vanadium pentoxide nanowires. *Adv. Mater.* **2000**, *12*, 420–424.

[29] Watanabe, T.; Ikeda, Y.; Ono, T.; Hibino, M.; Hosoda, M.; Sakai, K.; Kudo, T. Characterization of vanadium oxide sol as a starting material for high rate intercalation cathodes. *Solid State Ionics* **2002**, *151*, 313–320.

[30] Liu, Y. Y.; Clark, M.; Zhang, Q. F.; Yu, D. M.; Liu, D.; Liu, J. W.; Cao, G. Z. V_2O_5 nano-electrodes with high power and energy densities for thin film Li-ion batteries. *Adv. Energy Mater.* **2011**, *1*, 194–202.

[31] Raju, V.; Rains, J.; Gates, C.; Luo, W.; Wang, X. F.; Stickle, W. F.; Stucky, G. D.; Ji, X. L. Superior cathode of sodium-ion batteries: Orthorhombic V_2O_5 nanoparticles generated in nanoporous carbon by ambient hydrolysis deposition. *Nano Lett.* **2014**, *14*, 4119–4124.

[32] Varadaraajan, V.; Satishkumar, B. C.; Nanda, J.; Mohanty, P. Direct synthesis of nanostructured V_2O_5 films using solution plasma spray approach for lithium battery applications. *J. Power Sources* **2011**, *196*, 10704–10711.

[33] Ng, S. H.; Patey, T. J.; Büchel, R.; Krumeich, F.; Wang, J. Z.; Liu, H. K.; Pratsinis, S. E.; Novák, P. Flame spray-pyrolyzed vanadium oxide nanoparticles for lithium battery cathodes. *Phys. Chem. Chem. Phys.* **2009**, *11*, 3748–3755.

[34] Mai, L. Q.; Dong, F.; Xu, X.; Luo, Y. Z.; An, Q. Y.; Zhao, Y. L.; Pan, J.; Yang, J. N. Cucumber-like V_2O_5/poly(3,4-ethylenedioxythiophene)&MnO_2 nanowires with enhanced electrochemical cyclability. *Nano Lett.* **2013**, *13*, 740–745.

[35] Liu, H. M.; Yang, W. S. Ultralong single crystalline V_2O_5 nanowire/graphene composite fabricated by a facile green approach and its lithium storage behavior. *Energy Environ. Sci.* **2011**, *4*, 4000–4008.

[36] Wang, Y.; Takahashi, K.; Shang, H. M.; Cao, G. Z. Synthesis and electrochemical properties of vanadium pentoxide nanotube arrays. *J. Phys. Chem. B* **2005**, *109*, 3085–3088.

[37] Wang, H. Y.; Huang, K. L.; Huang, C. H.; Liu, S. Q.; Ren, Y.; Huang, X. B. $(NH_4)_{0.5}V_2O_5$ nanobelt with good cycling stability as cathode material for Li-ion battery. *J. Power Sources* **2011**, *196*, 5645–5650.

[38] Rui, X. H.; Lu, Z. Y.; Yu, H.; Yang, D.; Hng, H. H.; Lim, T. M.; Yan, Q. Y. Ultrathin V_2O_5 nanosheet cathodes: Realizing ultrafast reversible lithium storage. *Nanoscale* **2013**, *5*, 556–560.

[39] Mai, L. Q.; Xu, L.; Han, C. H.; Xu, X.; Luo, Y. Z.; Zhao, S. Y.; Zhao, Y. L. Electrospun ultralong hierarchical vanadium oxide nanowires with high performance for lithium ion batteries. *Nano Lett.* **2010**, *10*, 4750–4755.

[40] Yu, D. M.; Chen, C. G.; Xie, S. H.; Liu, Y. Y.; Park, K.; Zhou, X. Y.; Zhang, Q. F.; Li, J. Y.; Cao, G. Z. Mesoporous vanadium pentoxide nanofibers with significantly enhanced Li-ion storage properties by electrospinning. *Energy Environ. Sci.* **2011**, *4*, 858–861.

[41] Yan, J.; Sumboja, A.; Khoo, E.; Lee, P. S. V_2O_5 loaded on SnO_2 nanowires for high-rate Li ion batteries. *Adv. Mater.* **2011**, *23*, 746–750.

[42] Cao, A. M.; Hu, J. S.; Liang, H. P.; Wan, L. J. Self-assembled vanadium pentoxide (V_2O_5) hollow microspheres from nanorods and their application in lithium-ion batteries. *Angew. Chem. Int. Edit.* **2005**, *44*, 4391–4395.

[43] Sasidharan, M.; Gunawardhana, N.; Yoshio, M.; Nakashima, K.

V_2O_5 hollow nanospheres: A lithium intercalation host with good rate capability and capacity retention. *J. Electrochem. Soc.* **2012**, *159*, A618–A621.

[44] Wang, S. Q.; Lu, Z. D.; Wang, D.; Li, C. G.; Chen, C. H.; Yin, Y. D. Porous monodisperse V_2O_5 microspheres as cathode materials for lithium-ion batteries. *J. Mater. Chem.* **2011**, *21*, 6365–6369.

[45] Feng, C. Q.; Wang, S. Y.; Zeng, R.; Guo, Z. P.; Konstantinov, K.; Liu, H. K. Synthesis of spherical porous vanadium pentoxide and its electrochemical properties. *J. Power Sources* **2008**, *184*, 485–488.

[46] Liu, Y. Y.; Li, J. G.; Zhang, Q.; Zhou, N.; Uchaker, E. F.; Cao, G. Z. Porous nanostructured V_2O_5 film electrode with excellent Li-ion intercalation properties. *Electrochem. Commun.* **2011**, *13*, 1276–1279.

[47] An, Q. Y.; Wei, Q. L.; Mai, L. Q.; Fei, J. Y.; Xu, X.; Zhao, Y. L.; Yan, M. Y.; Zhang, P. F.; Huang, S. Z. Supercritically exfoliated ultrathin vanadium pentoxide nanosheets with high rate capability for lithium batteries. *Phy. Chem. Chem. Phys.* **2013**, *15*, 16828–16833.

[48] Liu, N.; Lu, Z. D.; Zhao, J.; McDowell, M. T.; Lee, H. W.; Zhao, W. T.; Cui, Y. A pomegranate-inspired nanoscale design for large-volume-change lithium battery anodes. *Nat. Nanotechnol.* **2014**, *9*, 187–192.

[49] Xiang, H. F.; Wang, H.; Chen, C. H.; Ge, X. W.; Guo, S.; Sun, J. H.; Hu, W. Q. Thermal stability of $LiPF_6$-based electrolyte and effect of contact with various delithiated cathodes of Li-ion batteries. *J. Power Sources* **2009**, *191*, 575–581.

[50] Sun, Y. K.; Oh, S. M.; Park, H. K.; Scrosati, B. Micrometer-sized, nanoporous, high-volumetric-capacity $LiMn_{0.85}Fe_{0.15}PO_4$ cathode material for rechargeable lithium-ion batteries. *Adv. Mater.* **2011**, *23*, 5050–5054.

[51] Sun, C. W.; Rajasekhara, S.; Goodenough, J. B.; Zhou, F. Monodisperse porous $LiFePO_4$ microspheres for a high power Li-ion battery cathode. *J. Am. Chem. Soc.* **2011,** *133*, 2132–2135.

[52] Ren, M. M.; Zhou, Z.; Gao, X. P.; Peng, W. X.; Wei, J. P. Core–shell $Li_3V_2(PO_4)_3$@C composites as cathode materials for lithium-ion batteries. *J. Phys. Chem. C* **2008**, *112*, 5689–5693.

[53] Liu, J.; Zhou, Y. C.; Wang, J. B.; Pan, Y.; Xue, D. F. Template-free solvothermal synthesis of yolk–shell V_2O_5 microspheres as cathode materials for Li-ion batteries. *Chem. Commun.* **2011**, *47*, 10380–10382.

[54] Xie, H. M.; Wang, R. S.; Ying, J. R.; Zhang, L. Y.; Jalbout, A. F.; Yu, H. Y.; Yang, G. L.; Pan, X. M.; Su, Z. M. Optimized $LiFePO_4$–polyacene cathode material for lithium-ion batteries. *Adv. Mater.* **2006**, *18*, 2609–2613.

[55] Pan, A. Q.; Wu, H. B.; Yu, L.; Zhu, T.; Lou, X. W. Synthesis of hierarchical three-dimensional vanadium oxide microstructures as high-capacity cathode materials for lithium-ion batteries. *ACS Appl. Mater. Interfaces* **2012**, *4*, 3874–3879.

[56] Kim, H.; Han, B.; Choo, J.; Cho, J. Three-dimensional porous silicon particles for use in high-performance lithium secondary batteries. *Angew. Chem. Int. Ed.* **2008**, *47*, 10151–10154.

[57] Zhang, C. F.; Chen, Z. X.; Guo, Z. P.; Lou, X. W. D. Additive-free synthesis of 3D porous V_2O_5 hierarchical microspheres with enhanced lithium storage properties. *Energy Environ. Sci.* **2013**, *6*, 974–978.

[58] Kang, L. T.; Fu, H. B.; Cao, X. Q.; Shi, Q.; Yao, J. N. Controlled morphogenesis of organic polyhedral nanocrystals from cubes, cubooctahedrons, to octahedrons by manipulating the growth kinetics. *J. Am. Chem. Soc.* **2011**, *133*, 1895–1901.

[59] Zhang, X. F.; Wang, K. X.; Wei, X.; Chen, J. S. Carbon-coated V_2O_5 nanocrystals as high performance cathode material for lithium ion batteries. *Chem. Mater.* **2011**, *23*, 5290–5292.

[60] Yu, H. D.; Wang, D. S.; Han, M. Y. Top-down solid-phase fabrication of nanoporous cadmium oxide architectures. *J. Am. Chem. Soc.* **2007**, *129*, 2333–2337.

[61] An, Q. Y.; Zhang, P. F.; Wei, Q. L.; He, L.; Xiong, F. Y.; Sheng, J. Z.; Wang, Q. Q.; Mai, L. Q. Top-down fabrication of three-dimensional porous V_2O_5 hierarchical microplates with tunable porosity for improved lithium battery performance. *J. Mater. Chem. A* **2014**, *2*, 3297–3302.

[62] Choi, B. G.; Chang, S. J.; Lee, Y. B.; Bae, J. S.; Kim, H. J.; Huh, Y. S. 3D heterostructured architectures of Co_3O_4 nanoparticles deposited on porous graphene surfaces for high performance of lithium ion batteries. *Nanoscale* **2012**, *4*, 5924–5930.

[63] Mahmood, N.; Zhang, C. Z.; Hou, Y. L. Nickel sulfi de/nitrogen-doped graphene composites: Phase-controlled synthesis and high performance anode materials for lithium ion batteries. *Small* **2013**, *9*, 1321–1328.

[64] Meng, F. L.; Fang, Z. G.; Li, Z. X.; Xu, W. W.; Wang, M. J.; Liu, Y. P.; Zhang, J.; Wang, W. R.; Zhao, D. Y.; Guo, X. H. Porous Co_3O_4 materials prepared by solid-state thermolysis of a novel Co-MOF crystal and their superior energy storage performances for supercapacitors. *J. Mater. Chem. A* **2013**, *1*, 7235–7241.

[65] Mahmood, N.; Zhang, C. Z.; Liu, F.; Zhu, J. H.; Hou, Y. L. Hybrid of Co_3Sn_2@Co nanoparticles and nitrogen-doped graphene as a lithium ion battery anode. *ACS nano* **2013**, *7*, 10307–10318.